Astronomy
&
Astrophysics

# Upper limits on CH$_3$OH in the HD 163296 protoplanetary disk

## Evidence for a low gas-phase CH$_3$OH-to-H$_2$CO ratio

M. T. Carney[1], M. R. Hogerheijde[1], V. V. Guzmán[2,3], C. Walsh[4], K. I. Öberg[5], E. C. Fayolle[6], L. I. Cleeves[7],
J. M. Carpenter[2], and C. Qi[5]

[1] Leiden Observatory, Leiden University, PO Box 9513, 2300 RA Leiden, The Netherlands
    e-mail: masoncarney@strw.leidenuniv.nl
[2] Joint ALMA Observatory (JAO), Alonso de Córdova 3107, Vitacura, Santiago de Chile, Chile
[3] Instituto de Astrofísica, Ponticia Universidad Católica de Chile, Av. Vicuña Mackenna 4860, 7820436 Macul, Santiago, Chile
[4] School of Physics and Astronomy, University of Leeds, Leeds LS2 9JT, UK
[5] Department of Astronomy, Harvard University, Cambridge, MA 02138, USA
[6] Jet Propulsion Laboratory, California Institute of Technology, 4800 Oak Grove Drive, Pasadena, CA 91109-8099, USA
[7] University of Virginia, Charlottesville, VA 22904, USA

**ABSTRACT**

*Context.* Methanol (CH$_3$OH) is at the root of organic ice chemistry in protoplanetary disks. Its connection to prebiotic chemistry and its role in the chemical environment of the disk midplane make it an important target for disk chemistry studies. However, its weak emission has made detections difficult. To date, gas-phase CH$_3$OH is detected in only one Class II disk, TW Hya.
*Aims.* We aim to constrain the methanol content of the HD 163296 protoplanetary disk.
*Methods.* We used the Atacama Large Millimeter/submillimeter Array (ALMA) to search for a total of four CH$_3$OH emission lines in bands six and seven toward the disk around the young Herbig Ae star HD 163296. The disk-averaged column density of methanol and its related species formaldehyde (H$_2$CO) were estimated assuming optically thin emission in local thermodynamic equilibrium. We compared these results to the gas-phase column densities of the TW Hya disk.
*Results.* No targeted methanol lines were detected with Keplerian masking in the image plane nor with matched filter analysis in the *uv* plane individually nor after line stacking. The $3\sigma$ disk-integrated intensity upper limits are <51 mJy km s$^{-1}$ for the band six lines and <26 mJy km s$^{-1}$ for the band seven lines. The band seven lines provide the strictest $3\sigma$ upper limit on disk-averaged column density with $N_{\rm avg} < 5.0 \times 10^{11}$ cm$^{-2}$. The methanol-to-formaldehyde ratio is CH$_3$OH/H$_2$CO <0.24 in the HD 163296 disk compared to a ratio of 1.27 in the TW Hya disk.
*Conclusions.* The HD 163296 protoplanetary disk is less abundant in methanol with respect to formaldehyde compared to the disk around TW Hya. Differences in the stellar irradiation in this Herbig Ae disk as compared to that of a disk around a T Tauri star likely influence the gaseous methanol and formaldehyde content. Possible reasons for the lower HD 163296 methanol-to-formaldehyde ratio include: a higher than expected gas-phase formation of H$_2$CO in the HD 163296 disk, uncertainties in the grain surface formation efficiency of CH$_3$OH and H$_2$CO, and differences in the disk structure and/or CH$_3$OH and H$_2$CO desorption processes that drive the release of the molecules from ice mantles back into the gas phase. These results provide observational evidence that the gas-phase chemical complexity found in disks may be strongly influenced by the spectral type of the host star.

**Key words.** astrochemistry – protoplanetary disks – submillimeter: stars

## 1. Introduction

Methanol is an astrobiologically relevant molecule because it acts as a precursor to more complex organic molecules (COMs) that may develop into amino acids and other building blocks of life (Öberg et al. 2009; Herbst & van Dishoeck 2009). Maintaining an understanding of methanol chemistry through the numerous stages of star and planet formation is essential to make predictions on the molecular complexity available for incorporation into extrasolar planetary bodies (e.g., Drozdovskaya et al. 2014). The CH$_3$OH molecule is regularly detected in the earlier, embedded stages of star formation both in the solid phase through ice absorption (Grim et al. 1991; Skinner et al. 1992; Dartois et al. 1999; Pontoppidan et al. 2004; Bottinelli et al. 2010; Kristensen et al. 2010; Shimonishi et al. 2010; Boogert et al. 2015) and in the gas phase (Friberg et al. 1988;

van Dishoeck et al. 1995; Graninger et al. 2016; Lee et al. 2017). These observations provide evidence for the presence of CH$_3$OH ices in cold molecular clouds and protostellar envelopes.

To date, methanol is detected in two protoplanetary disks: the Class II TW Hydrae (Walsh et al. 2016) and the younger Class I V883 Orionis, an outbursting FU Orionis object (van 't Hoff et al. 2018). There are currently few informative upper limits on gas-phase methanol in disks. The reason for the apparent absence of gas-phase methanol in protoplanetary disks is not immediately obvious because CH$_3$OH is expected to form via the hydrogenation of CO ices (Watanabe et al. 2003; Cuppen et al. 2009) on the surface of dust grains. Also, the colder, outer regions of protoplanetary disks are expected to inherit a reservoir of methanol ice formed earlier, during the protostellar or interstellar phase. Methanol is produced by the same grain surface formation pathway as formaldehyde, which is readily detected in disks in the

gas phase (Aikawa et al. 2003; Öberg et al. 2010, 2017; Qi et al. 2013; van der Marel et al. 2014; Loomis et al. 2015; Carney et al. 2017). However, because of the much higher methanol binding (desorption) energy (e.g., $E_{des}$ of ~2000 K for $H_2CO$ and ~ 5500 K for $CH_3OH$ in mixtures of water ice; Collings et al. 2004; Garrod & Herbst 2006), methanol is expected to be frozen out over a much larger region of the disk than formaldehyde.

Variation in the formaldehyde and methanol content across protoplanetary disks may point to differences in their formation processes. Formaldehyde can be formed in the gas phase and on grain surfaces, therefore a lower than expected methanol-to-formaldehyde ratio could be due to a more efficient gas-phase pathway to form $H_2CO$ (Fockenberg & Preses 2002; Atkinson et al. 2006), less efficient conversion of $H_2CO$ into $CH_3OH$ on grain surfaces than expected, or lower than expected $CH_3OH$ photodesorption rates and/or immediate UV photodissociation of gas-phase $CH_3OH$ (Bertin et al. 2016; Cruz-Diaz et al. 2016).

The HD 163296 (MWC 275) system is an ideal testbed in which to explore chemical processing in protoplanetary disks, in particular for organics. It is an isolated Herbig Ae pre-main sequence (PMS) star with spectral type A2Ve at an age of ~5 Myr (Alecian et al. 2013). The star is surrounded by a large, bright protoplanetary disk containing a significant reservoir of gas that extends out to ~550 AU in the gas based on CO measurements (de Gregorio-Monsalvo et al. 2013). The disk has an inclination of 44°, a position angle of 133°, and a total mass of $M_{disk} \approx 0.09\,M_\odot$ based on physical models (Qi et al. 2011; Rosenfeld et al. 2013). At such an inclination, the vertical structure as well as the radial structure can be inferred directly from the molecular line emission maps (Rosenfeld et al. 2013; Flaherty et al. 2015).

Recent measurements of the stellar parallax by *Gaia* put the HD 163296 system at a distance of $d = 101 \pm 1$ pc (Gaia Collaboration 2018), significantly closer than previous distance estimates of 122 pc (van den Ancker et al. 1998)[1]. While the new distance will affect the stellar parameters, this work adopts the previously reported values for stellar mass (2.3 $M_\odot$; Qi et al. 2011) and distance ($d = 122$ pc). The analysis presented here focuses on the disk-averaged molecular column density ratios of methanol and formaldehyde within the same disk. The column density is derived from the disk-integrated line flux, therefore the updated *Gaia* distance measurements will affect the line flux similarly for molecular species within the same disk, and the effect of the new distance is canceled out.

The proximity and size of the disk combined with the high total luminosity of the Herbig Ae PMS star provides a unique opportunity to fully resolve the location of the CO snow line, that is, the midplane radius beyond which gas-phase CO will freeze out into ice (Qi et al. 2011, 2015; Mathews et al. 2013). Current estimates by Qi et al. (2015) place the CO snow line at a midplane radius of 90 AU, corresponding to a gas and dust temperature of ~24 K in this disk. Recent work has revealed that the disk consists of several rings and gaps in the millimeter dust and in the gas (Isella et al. 2016), while the CO gas shows asymmetries at specific velocities (Pinte et al. 2018; Teague et al. 2018), both of which may be indicative of planet-disk interaction from embedded forming planets. Given its large radial extent of ~550 AU and

resolved, relatively close-in CO snow line position, HD 163296 is one of the best candidates to probe the formation of organics that require the freeze-out of abundant volatiles such as CO.

This paper presents observations from the Atacama Large Millimeter/submillimeter Array (ALMA) of the $CH_3OH$ molecule toward HD 163296. Section 2 describes the observations and data reduction. Results including the upper limits on the methanol content of the HD 163296 disk and a comparison to the TW Hya disk are described in Sect. 3. In Sect. 4 we discuss the implications of the upper limits and the detectability of methanol in disks similar to HD 163296. Section 5 presents the conclusions of this work.

## 2. Observations and reduction

HD 163296 (J2000: RA = $17^h56^m21.280^s$, Dec = $-21°57'22.441''$) was observed with ALMA in band six and band seven during Cycle 4 under project 2016.1.00884.S. Band six and band seven are receivers operating in the 211–275 GHz and 275–373 GHz range, respectively. Band six observations were done with the ALMA 12-m array on 2016 November 11, 2016 December 01, and 2017 March 15 with 42 antennas. Band seven observations were carried out with the Atacama Compact Array (ACA) on 2016 October 05, 08, 13, 26 using 10 of the 7-m ACA antennas, and with the ALMA 12-m array on 2017 April 13 using 45 antennas. In total, four transitions of $CH_3OH$ were targeted across the two bands with the frequency domain mode (FDM) correlator setting: two $CH_3OH$ $5_{05}-4_{04}$ (A/E) lines[2] in band six at 241.791 and 241.700 GHz with a frequency (velocity) resolution of 244 kHz (0.303 km s$^{-1}$); and in band seven, $CH_3OH$ $2_{11}-2_{02}$ (A) at 304.208 GHz and $CH_3OH$ $1_{10}-1_{01}$ (A) at 303.367 GHz with a frequency (velocity) resolution of 141 kHz (0.139 km s$^{-1}$). All $CH_3OH$ lines were in the upper side band (USB) of their execution blocks. The lower side band (LSB) contained observations of the continuum, $C^{17}O$ $J = 2-1$, CN $J = 2-1$, and $CH_3CN$ $J = 13-12$ in band six, and the continuum, DCN $J = 4-3$, and four $H_2CO$ lines in band seven which will be presented in Guzmán et al. (in prep.). Table 1 summarizes the observational parameters for each $CH_3OH$ line and the continuum.

Band six observations were obtained over three execution blocks with 6.05 s integration steps and 68 min total time on-source. System temperatures varied from 60–140 K and the average precipitable water vapor varied from 1.5–2.3 mm. J1924-2914 was the bandpass calibrator and Titan was the flux calibrator for all execution blocks. The average flux values for Titan were: 1.15 Jy in the USB and 1.01 Jy in the LSB for 2016 November 11 and December 01; 0.963 Jy in the USB and 0.846 Jy in the LSB for 2017 March 15. The gain calibrator was different for each execution block: J1745-2900 on 2016 November 11, J1742-1517 on 2016 December 01, and J1733-1304 on 2017 March 15. The derived flux values for J1745-2900, J1742-1517, and J1733-1304 were 3.29, 0.212, and 1.47 Jy, respectively. All measurement sets were subsequently concatenated and time binned to 30 s integration time per visibility for imaging and analysis.

Band seven observations were obtained with the 12-m array over three execution blocks with 6.05 s integration steps and

---

[1] The updated distance $d = 101 \pm 1$ pc results in a stellar luminosity of ~23 $L_\odot$, which is 30% lower than the previous estimate (Alecian et al. 2013). Applying the adjusted luminosity value to the H–R diagram used by Alecian et al. (2013) to determine the age of the system and stellar mass results in an updated age of ~9 Myr and an adjusted stellar mass closer to 2.1 $M_\odot$.

[2] As a methyl group molecule, methanol exists in three forms with different hydrogen spin symmetry properties. The A-type form has a total spin 3/2, while the E-type form is degenerate having $E^a$ and $E^b$ varieties with total spin 1/2. The ratio of A-type to E-type forms of methanol is one.

**Table 1.** HD 163296 observational parameters.

|  | Band 6 | |
| --- | --- | --- |
| Dates observed | 2016 November 11, December 01; 2017 March 15 | |
| Baselines | 15–1000 m \| 12–776 k$\lambda$ | |
|  | CH$_3$OH $5_{05}$–$4_{04}$ (E) | CH$_3$OH $5_{05}$–$4_{04}$ (A) |
| Rest frequency (GHz) | 241.700 | 241.791 |
| Synthesized beam (*FWHM*) | 1.46″ × 1.13″ | 1.46″ × 1.13″ |
| Position angle | −76.6° | −76.6° |
| Channel width (km s$^{-1}$) | 0.303 | 0.303 |
| rms noise[a] (mJy beam$^{-1}$) | 3.0 | 3.0 |
| Weighting | Natural | Natural |
| Continuum frequency (GHz) | 233.0 | |
| Synthesized beam (*FWHM*) | 0.55″ × 0.37″ | |
| Position angle | 76.8° | |
| rms noise (mJy beam$^{-1}$) | 0.17 | |
| Integrated flux (mJy) | 754 ± 75 | |
| Weighting | Briggs, robust = 0.5 | |
|  | Band 7 | |
| Dates observed | ACA | 2016 October 05, 08, 13, 26 |
|  | 12-m array | 2017 April 13 |
| Baselines | ACA | 9–49 m \| 9–48 k$\lambda$ |
|  | 12-m array | 15–460 m \| 15–454 k$\lambda$ |
|  | CH$_3$OH $1_{10}$–$1_{01}$ (A) | CH$_3$OH $2_{11}$–$2_{02}$ (A) |
| Rest frequency (GHz) | 303.367 | 304.208 |
| Synthesized beam (*FWHM*) | 1.37″ × 1.14″ | 1.36″ × 1.15″ |
| Position angle | 91.1° | 90.6° |
| Channel width (km s$^{-1}$) | 0.139 | 0.139 |
| rms noise[a] (mJy beam$^{-1}$) | 2.5 | 2.5 |
| Weighting | Natural | Natural |
| Continuum frequency (GHz) | 296.0 | |
| Synthesized beam (*FWHM*) | 0.63″ × 0.48″ | |
| Position angle | 87.8° | |
| rms noise (mJy beam$^{-1}$) | 0.09 | |
| Integrated flux (mJy) | 1288 ± 128 | |
| Weighting | Briggs, robust = 0.5 | |

**Notes.** Flux calibration accuracy is taken to be 10%. Table 2 shows details for the line transition data. [a]Noise levels are per image channel.

105 min total time on-source. Data was also obtained with the ACA over four execution blocks with 10.1 s integration steps and 184 min total time on-source. System temperatures varied from 80–150 K and the average precipitable water vapor varied from 0.5–1.1 mm. J1924-2914 was the bandpass calibrator for all execution blocks. Titan, Neptune, J1733-1304, and J1751+0939 were used as flux calibrators. The average flux values were: Titan – 1.96 Jy in the USB and 1.82 Jy in the LSB for 2017 April 13; Neptune – 22.5 Jy in the USB and 21.2 Jy in the LSB for 2016 October 08, 26; J1733-1304 – 1.32 Jy (2017 April 13), 1.14 Jy (2016 October 13) in the USB and 1.36 Jy (2017 April 13), 1.18 Jy (2016 October 13) in the LSB; J1751+0939 – 1.58 Jy in the USB and 1.60 Jy in the LSB for 2016 October 05. The gain calibrators were J1733-1304 for the 12-m array data and J1745-2900 for the ACA data. The derived flux value for J1733-1304 was 1.36 Jy (2017 April 13) and the values for J1745-2900 were 3.2 Jy (2016 October 05, 08, 13), and 4.6 Jy (2016 October 26). All measurement sets were subsequently concatenated and time binned to 30 s integration time per visibility for imaging and analysis.

Self-calibration for HD 163296 in band six was done with five spectral windows dedicated to continuum observations: two in the LSB at 223.5 and 224 GHz and three in the USB at 234, 241, and 242 GHz with a total combined bandwidth of 469 MHz. The band six reference antenna was DA41. Band seven self-calibration was done with three spectral windows dedicated to continuum observations: one in the LSB at 289 GHz and two in the USB at 302 and 303.5 GHz with a total combined bandwidth of 469 MHz. The band seven reference antenna was DA59 for the 12-m array and CM03 for the ACA. A minimum of four baselines per antenna and a minimum signal-to-noise ratio (S/N) of two were required for self-calibration. Calibration solutions were calculated twice for phase and once for amplitude. The first phase solution interval (solint) was 200 s, the second phase and amplitude solutions had solint equal to the binned integration time (30 s). Self-calibration solutions for the continuum spectral windows were mapped to the line spectral windows nearest in frequency. Continuum subtraction for the line data was done in the *uv* plane using a single-order polynomial fit to the line-free channels. CLEAN imaging was performed with

natural weighting for each continuum-subtracted $CH_3OH$ line with a *uv* taper to achieve a 1″ beam in order to increase the sensitivity.

This paper also makes use of Submillimeter Array (SMA) $H_2CO$ data for the HD 163296 disk (Qi et al. 2013), ALMA $H_2CO$ data for the HD 163296 disk (Carney et al. 2017), ALMA $H_2CO$ data for the TW Hya disk (Öberg et al. 2017), and ALMA $CH_3OH$ data for the TW Hya disk (Walsh et al. 2016). The following software and coding languages are used for data analysis: the CASA package version 4.7.2 (McMullin et al. 2007) and PYTHON.

## 3. Results

No methanol lines listed in Table 1 are detected in the disk around HD 163296 neither individually nor after line stacking. In this section, we first describe the stacking and masking methods used to maximize the S/N to attempt to extract the disk-integrated intensity of the $CH_3OH$ lines. The method used to estimate the column density and abundance of methanol in the HD 163296 disk is then described. A comparison is presented between the $CH_3OH$ and $H_2CO$ content in the disks around HD 163296 and TW Hya based on data taken from the literature. Finally, model spectra of the band seven $CH_3OH$ lines are created for HD 163296 and compared to the sensitivity of the observations.

### 3.1. Line extraction

We attempted to extract the targeted $CH_3OH$ lines from the CLEAN image cubes using a circular aperture with an 8″ diameter centered on the source, which yielded no detections (Fig. 1). To increase the S/N we repeated this analysis after stacking the $CH_3OH$ lines using different line stacking schemes. We further attempted to increase the S/N of the $CH_3OH$ data by applying masking techniques: Keplerian masking in the image plane, and matched filter analysis in the *uv* plane to search for any signal in the raw visibilities.

#### 3.1.1. Line stacking

Stacking was done for band six and band seven lines separately, and then again for both bands together. The band seven lines are more easily excited due to their lower upper energy ($E_u < 22$ K) values compared to the band six lines ($E_u > 34$ K; Table 2), thus band seven observations should be sensitive to lower $CH_3OH$ column densities and should be easier to detect. We note that the level populations are likely to be in local thermodynamic equilibrium (LTE) for the expected methanol emitting region where gas densities in the disk are high ($\gtrsim 10^7$ cm$^{-3}$), thus we do not expect the critical density of the lines to influence the amount of line emission (Table 2).

First, we stacked the lines in the image plane by adding together the integrated intensity maps ($v = 2.4$–$9.2$ km s$^{-1}$) created from the $CH_3OH$ continuum-subtracted and *uv*-tapered CLEAN image cubes. Second, we stacked in the *uv* plane by concatenating ALMA measurement sets prior to imaging. Stacking in the *uv* plane was done using the CASA cvel function, which was used to regrid the velocity axis of line data and has the option to combine visibility data for multiple lines. For *uv* stacking across all bands, the band seven lines were regridded to 0.303 km s$^{-1}$ channels to match the channel width of the band six lines. Methanol remains undetected after implementing the stacking methods described above.

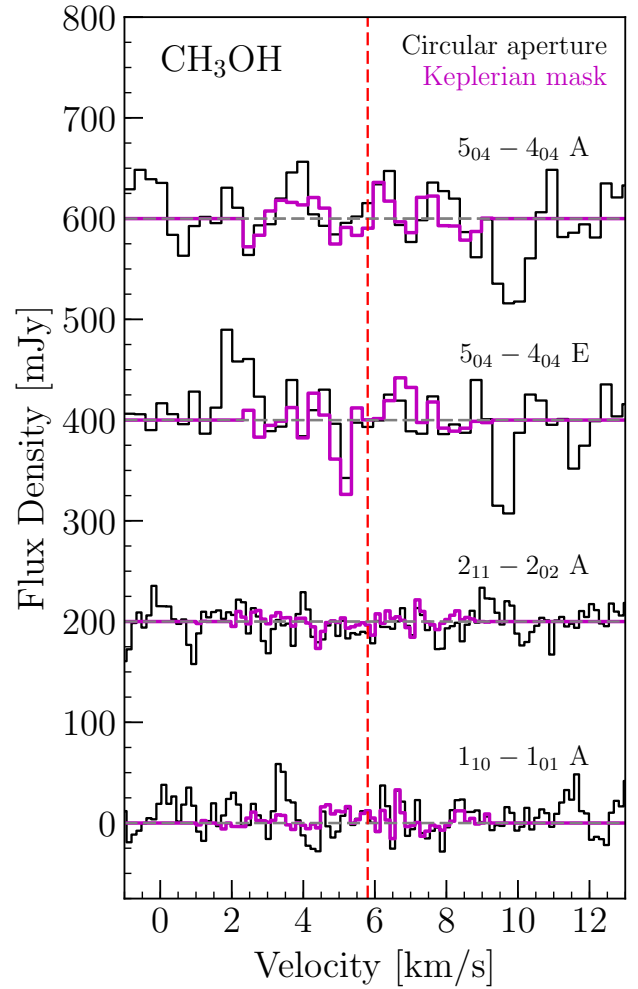**Fig. 1.** Spectra at the expected velocity of $CH_3OH$ line emission in the HD 163296 disk showing non-detections from aperture-masked image cubes using an 8″ diameter circular aperture (black) and Keplerian-masked image cubes (magenta). The two bottom spectra are observed in band seven in 0.139 km s$^{-1}$ channels while the two top spectra are in band six in 0.303 km s$^{-1}$ channels. The horizontal gray dashed line represents the spectrum baseline, which is offset by 200 mJy for each line. The vertical red dashed line shows the systemic velocity at 5.8 km s$^{-1}$ (Qi et al. 2011).

#### 3.1.2. Keplerian masking in the image plane

For maximum S/N in the image plane, we applied a Keplerian mask to the CLEAN image cube for each $CH_3OH$ line (Carney et al. 2017; Salinas et al. 2017) to exclude noisy pixels that are not associated with the emission expected from a disk in Keplerian rotation. The mask is based on the velocity profile of a rotating disk, which is assumed to be Keplerian around a central stellar mass of $M = 2.3$ $M_\odot$ (Alecian et al. 2013). A subset of pixels $(x, y, v)$ are identified in the $CH_3OH$ image cubes where the Doppler-shifted line velocity projected along the line of sight matches the pixel Keplerian velocity $(x, y, v_K)$ projected along the line of sight. Pixels with velocities that do not match the Keplerian rotational profile criteria are masked. Integrated intensity maps and disk-integrated spectra were again created from the Keplerian-masked cubes of the $CH_3OH$ lines individually and after line stacking; however, in all cases, $CH_3OH$ remains undetected. Figure 1 shows the aperture-masked spectra and the Keplerian-masked spectra of the four methanol lines targeted in HD 163296.

**Table 2.** Disk-averaged column density and abundance of CH$_3$OH in HD 163296 and TW Hya.

| Object | Line | $\int I_\nu \mathrm{d}\nu^a$ (mJy km s$^{-1}$) | $E_u$ (K) | $\log(A_{ul})$ (s$^{-1}$) | $n_{crit}$ (cm$^{-3}$) | $N_{avg}$ (cm$^{-2}$) | CH$_3$OH/H$_2$ |
|---|---|---|---|---|---|---|---|
| HD 163296 | CH$_3$OH $5_{05}$–$4_{04}$ (E) | <51 | 47.9 | −4.22 | 1.6(06) | <6.9(12) | <2.1(−11) |
| | CH$_3$OH $5_{05}$–$4_{04}$ (A) | <51 | 34.8 | −4.22 | 4.3(05) | <4.1(12) | <1.3(−11) |
| | CH$_3$OH $1_{10}$–$1_{01}$ (A) | <26 | 16.9 | −3.49 | 4.3(07) | <7.0(11) | <2.2(−12) |
| | CH$_3$OH $2_{11}$–$2_{02}$ (A) | <26 | 21.6 | −3.49 | 5.0(06) | <5.0(11) | <1.6(−12) |
| TW Hya | CH$_3$OH stacked$^b$ | 26.5 ± 2.7 | 28.6 | −3.49 | 3.0(06) | 4.7(12) | 1.1(−12) |

**Notes.** The disk-averaged column density is calculated using Eq. (1) with $T_{ex} = 25$ K. The format $a(b)$ translates to $a \times 10^b$. Flux errors are dominated by systematic uncertainties, taken to be 10%. $^{(a)}$Upper limits are derived at the $3\sigma$ level using the HD 163296 Keplerian mask (Sect. 3). $^{(b)}$The stacked detection consists of three CH$_3$OH transitions: CH$_3$OH $2_{11}$–$2_{02}$ (A) at 304.208 GHz, CH$_3$OH $3_{12}$–$3_{03}$ (A) at 305.472 GHz, and CH$_3$OH $4_{13}$–$4_{04}$ (A) at 307.166 GHz. Excitation parameters for the CH$_3$OH $3_{12}$–$3_{03}$ (A) line are used to calculate column density.
**References.** Rabli & Flower (2010); Walsh et al. (2016).

Upper limits on the integrated intensity for each CH$_3$OH line were calculated using the projected Keplerian mask $(x, y, v_K)$ derived for the HD 163296 disk. To obtain the strictest upper limits on the integrated line intensity, we included only the positions and velocities associated with the disk. Therefore, the mask cube contains pixels set equal to unity for $(x, y, v_K)$ positions only, and all other pixels are set to zero. The upper limit is set at $3\sigma$ where $\sigma = \delta v \sqrt{N} \sigma_{rms}$, $\delta v$ is the velocity channel width in km s$^{-1}$, $N$ is the number of independent measurements contained within the projected Keplerian mask, and $\sigma_{rms}$ is the rms noise per channel in mJy beam$^{-1}$ (Table 1). To account for correlated noise within the size of the beam, we summed over all $(x, y, v_K)$ pixel positions and divide by the number of pixels per beam $n_{ppb}$, to get $N = \Sigma(x, y, v_K)/n_{ppb}$, the number of independent measurements over the integrated Keplerian mask. The disk-integrated upper limits for each CH$_3$OH line are listed in Table 2.

### 3.1.3. Matched filter analysis in the *uv* plane

To maximize the S/N in the *uv* plane, we applied a matched filter to the CH$_3$OH line visibility data (Loomis et al. 2018). In this technique, a template image cube is sampled in *uv* space to obtain a set of template visibilities that act as the filter. The filter is then cross-correlated with a set of low S/N visibilities (in this case, the CH$_3$OH data) in an attempt to detect any signal that is co-spatial with the template emission. Loomis et al. (2018) and Carney et al. (2017) have published positive detections using the matched filter technique for CH$_3$OH and H$_2$CO, which can provide an improvement in S/N of >50–500% over the traditional aperture masking, depending on the spectral resolution of the observed visibilities.

We used the H$_2$CO $3_{03}$–$2_{02}$ detection toward the HD 163296 disk reported in Carney et al. (2017) as the template emission profile under the assumption that CH$_3$OH and H$_2$CO reside in similar regions. The emission morphologies will be dominated primarily by Keplerian rotation, therefore a high degree of co-spatiality is expected. The H$_2$CO line was re-imaged with CLEAN to achieve a spatial and spectral resolution equal to the observed CH$_3$OH lines. Channels with H$_2$CO emission ($v = 1.6$–$10$ km s$^{-1}$) are sampled in *uv* space using the PYTHON vis_sample$^3$ routine. The matched filter was run for the CH$_3$OH line visibility data individually and after line stacking.

$^3$ vis_sample is publicly available at https://github.com/AstroChem/vis_sample or in the Anaconda Cloud at https://anaconda.org/rloomis/vis_sample

Figure 2 shows the spectrum that is produced by the matched filter analysis for the band seven CH$_3$OH data. The filter response in units of $\sigma$ is the measure of the S/N of the cross-correlation between the CH$_3$OH line visibility data and the filter derived from the template H$_2$CO emission. A correlation between the CH$_3$OH data and the filter would result in a peak at the source velocity. No such feature is seen in the filter response spectrum of any CH$_3$OH lines in the HD 163296 disk, suggesting that the detection threshold for methanol is well below the sensitivity achieved in our ALMA observations. The matched filter analyses confirm the non-detection of CH$_3$OH found during analysis in the image plane. The same analysis for the band six lines also results in no detection, which is expected given that the band seven lines should be brighter.

### 3.2. CH$_3$OH column density and abundance upper limits

We calculated the disk-averaged column density of CH$_3$OH based on the integrated line intensity upper limit, an assumed excitation temperature, and the total disk mass. Following the formula used by Remijan et al. (2003) and Miao et al. (1995) for optically thin emission in local thermodynamic equilibrium (LTE), we can estimate the column density

$$N = 2.04 \frac{\int I_\nu \mathrm{d}v}{\theta_a \theta_b} \frac{Q_{rot} \exp(E_u/T_{ex})}{\nu^3 \langle S_{ul}\mu^2 \rangle} \times 10^{20} \text{ cm}^{-2}, \quad (1)$$

where $\int I_\nu \mathrm{d}v$ is the integrated line intensity in Jy beam$^{-1}$ km s$^{-1}$, $\theta_a$ and $\theta_b$ correspond to the semi-major and semi-minor axes of the synthesized beam in arcseconds, $T_{ex}$ is the excitation temperature in K, and $\nu$ is the rest frequency of the transition in GHz. The partition function ($Q_{rot}$), upper energy level ($E_u$, in K), and the temperature-independent transition strength and dipole moment ($S_{ul}\mu^2$, in debye$^2$) for CH$_3$OH are taken from the Cologne Database for Molecular Spectroscopy (CDMS; Müller et al. 2005).

Methanol is expected to form primarily in ice in cold regions of protoplanetary disks, where gas densities are higher ($\sim 10^9$ cm$^{-3}$; Walsh et al. 2014) than the critical density of the observed CH$_3$OH transitions ($10^6$–$10^7$ cm$^{-3}$; Rabli & Flower 2010). Recent physical models of the HD 163296 disk have gas densities $>10^6$ cm$^{-3}$ in the region $z/r < 0.4$ (Qi et al. 2011; de Gregorio-Monsalvo et al. 2013; Rosenfeld et al. 2013), where $z$ and $r$ are the disk height and radius, respectively. In recent models of the TW Hya disk, Walsh et al. (2016) vary the methanol emitting region over the range $z/r < 0.1$, $0.1 < z/r < 0.2$, and
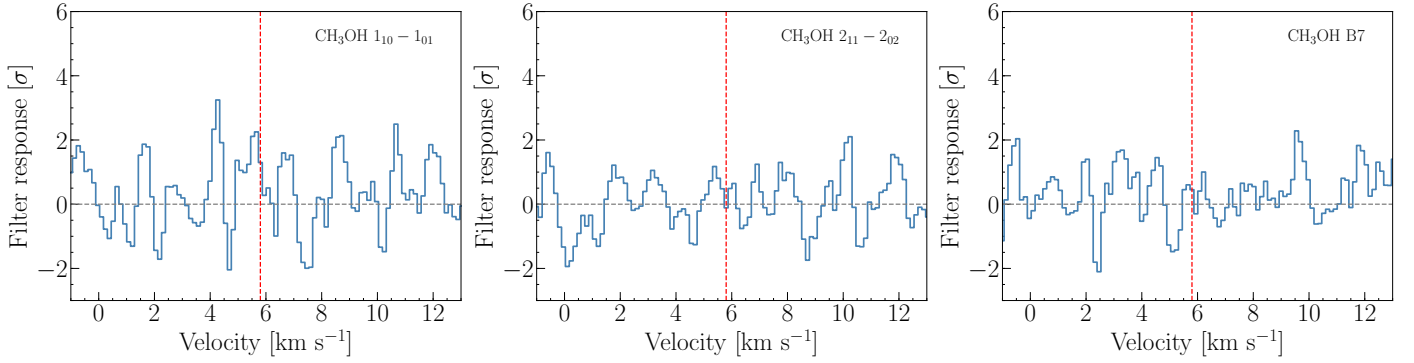
**Fig. 2.** Matched filter results for the band seven $CH_3OH$ lines in the HD 163296 disk using the $H_2CO$ emission as a template. A peak $>3\sigma$ at the source velocity ($v = 5.8$ km s$^{-1}$; red dashed line) would signify a positive detection of methanol. The band seven lines should be the strongest in our sample, but there is no evidence of $CH_3OH$ in the matched filter for the band seven individual lines nor the band seven stacked lines. *Left panel*: $CH_3OH$ $1_{10}-1_{01}$ (A) line. *Middle panel*: $CH_3OH$ $2_{11}-2_{02}$ (A) line. *Right panel*: stacked band seven $CH_3OH$ lines.

$0.2 < z/r < 0.3$, which all fit the data equally well. These models all have methanol present at $z/r < 0.3$, suggesting that emission is arising from dense regions within the disk. Under these conditions, LTE is a reasonable assumption, and thus $T_{ex}$ is expected to equal the kinetic temperature of the gas.

Assuming optically thin emission, the disk-averaged column density can be used to estimate the total number of $CH_3OH$ molecules in the disk $N(CH_3OH) = N_{avg}(a \times b)$, where $(a \times b)$ is the total emitting area of the disk. Assuming the total disk mass is primarily molecular hydrogen, we can estimate the total number of $H_2$ molecules $N(H_2) = M_{disk}/m_{H_2}$, where $m_{H_2}$ is the molecular hydrogen mass. The $CH_3OH$ emitting area was set to $a = b = 7''$ based on the $H_2CO$ emission diameter in the HD 163296 disk (Carney et al. 2017), assuming a similar chemical origin and distribution. The total disk mass is ~0.09 $M_\odot$ based on models of CO observations (Qi et al. 2011; Rosenfeld et al. 2013). Table 2 shows the disk-averaged column density and abundance for the single temperature assumption $T_{ex} = 25$ K in LTE, which is approximately the same as the excitation temperature found for $H_2CO$ in the HD 163296 disk (Qi et al. 2013; Carney et al. 2017). The $CH_3OH$ $2_{11}-2_{02}$ (A) line provides the strictest upper limit on the methanol column density and abundance in HD 163296, with $N_{avg} \lesssim 5.0 \times 10^{11}$ cm$^{-2}$ and $CH_3OH/H_2 \lesssim 1.6 \times 10^{-12}$, based on its disk-integrated line intensity upper limit and assuming an excitation temperature of $T_{ex} = 25$ K. Table A.1 shows the disk-averaged column density and abundance for a range of LTE excitation conditions with $T_{ex} = 25$, 50, and 75 K. The abundances do not vary with $T_{ex}$ by more than a factor of 2–3 in the most extreme cases.

### 3.3. $CH_3OH$ and $H_2CO$ in HD 163296 and TW Hya

We estimated the fraction of methanol relative to formaldehyde in the HD 163296 disk, based on our upper limits for $CH_3OH$, and in the TW Hya disk, the only Class II protoplanetary disk for which there is a gas-phase methanol detection (Walsh et al. 2016). Integrated line intensities for $H_2CO$ detections in HD 163296 and TW Hya were taken from the literature, and their disk-averaged column densities and abundances were derived in the same manner as described in Sect. 3.2 to ensure consistency when comparing the $H_2CO$ and $CH_3OH$ content. The TW Hya disk mass is 0.05 $M_\odot$ based on observations of the HD molecule (Bergin et al. 2013). The emitting area for $H_2CO$ in TW Hya was set to $a = b = 3''$ based on the diameter of emission observed by Öberg et al. (2017). The same $3''$

emitting area was used for $CH_3OH$ in TW Hya. Table 3 shows the calculated column densities and abundances for the $H_2CO$ observations.

For HD 163296, the $CH_3OH$ $2_{11}-2_{02}$ (A) line was used to calculate the methanol-to-formaldehyde ratio as it gives the strictest upper limits on the methanol abundance. For TW Hya, we obtained the integrated line intensity of the stacked methanol detection by Walsh et al. (2016), assumed that the majority of emission is due to the strongest individual line ($CH_3OH$ $3_{12}-3_{03}$ (A) at 305.473 GHz with $E_u = 28.6$ K; Walsh et al. 2014; Loomis et al. 2018), and used the excitation parameters of that line with Eq. (1) to derive the TW Hya $CH_3OH$ column density and abundance, and subsequently the methanol-to-formaldehyde ratio for the disk.

Results for $CH_3OH/H_2CO$ in TW Hya and HD 163296 can be found in Table 3. Ratios calculated with the $H_2CO$ $3_{12}-2_{11}$ line should be representative of the true methanol-to-formaldehyde ratio since the $H_2CO$ $3_{12}-2_{11}$ upper energy level ($E_u$), Einstein A coefficient ($A_{ul}$), and critical density ($n_{crit}$) are similar to that of the band seven methanol lines observed in these disks. Thus, we obtain $CH_3OH/H_2CO < 0.24$ for HD 163296 and 1.27 for TW Hya, which suggests that the disk around HD 163296 is less abundant in methanol relative to formaldehyde compared to the TW Hya disk.

### 3.4. Model $CH_3OH$ spectra for HD 163296

In addition to the extraction methods described in previous sections, we also attempted a forward modeling approach to interpret the $CH_3OH$ non-detections toward HD 163296. We modeled the HD 163296 $CH_3OH$ band seven spectra using a parameterized disk structure and radiative transfer methods in order to compare the modeled emission to the noise level in the Keplerian-masked image cubes. We adopted the physical structure and the abundance structure of the model used by Carney et al. (2017) to reproduce ALMA observations of $H_2CO$ in the HD 163296 disk, then scaled the $CH_3OH$ abundance with respect to the $H_2CO$ abundance. The Line Modeling Engine (LIME; Brinch & Hogerheijde 2010) 3D radiative transfer code was run in LTE with 10000 grid points at the source distance of the original Qi et al. (2011) physical model ($d = 122$ pc) to create synthetic images of the $CH_3OH$ observations. The synthetic images were continuum-subtracted, sampled in *uv* space with the PYTHON `vis_sample` routine, and imaged with CLEAN at the same velocity resolution as the observations.

**Table 3.** Disk-averaged column density and abundance of H$_2$CO in HD 163296 and TW Hya.

| Object | Line | $\int I_\nu \mathrm{d}\nu$ (mJy km s$^{-1}$) | $E_\mathrm{u}$ (K) | $\log(A_\mathrm{ul})$ (s$^{-1}$) | $n_\mathrm{crit}$ (cm$^{-3}$) | $N_\mathrm{avg}$ (cm$^{-2}$) | H$_2$CO/H$_2$ | CH$_3$OH/H$_2$CO[a] |
|---|---|---|---|---|---|---|---|---|
| HD 163296 | H$_2$CO $3_{12}$–$2_{11}$ | $890 \pm 89$ | 33.4 | $-3.55$ | 5.7(06) | 2.1(12) | 6.3(−12) | <0.24 |
| TW Hya | H$_2$CO $3_{12}$–$2_{11}$ | $291 \pm 29$ | 33.4 | $-3.55$ | 5.7(06) | 3.7(12) | 8.9(−13) | $1.27 \pm 0.13$ |

**Notes.** The disk-averaged column density was calculated using Eq. (1) with $T_\mathrm{ex} = 25$ K. The format $a(b)$ translates to $a \times 10^b$. Flux errors are dominated by systematic uncertainties, taken to be 10%. [a]Ratios are determined using the CH$_3$OH disk-integrated column density from Table 2. HD 163296: based on the strictest upper limit from the CH$_3$OH $2_{11}$–$2_{02}$ (A) line. TW Hya: based on the stacked CH$_3$OH detection.
**References.** Wiesenfeld & Faure (2013); Qi et al. (2013); Öberg et al. (2017).

Figure 3 shows the disk-integrated model spectra for the CH$_3$OH band seven lines for a range of methanol-to-formaldehyde ratios, as indicated by the legend. The spectra show that a line should have been detected in the disk around HD 163296 for CH$_3$OH/H$_2$CO $\approx 0.2$ for the most sensitive case (stacked band seven lines). This result is consistent with the upper limit on this ratio derived from the integrated intensity of the Keplerian mask cube as presented in Sect. 3.3.

## 4. Discussion

The results presented in Table 3 suggest that the HD 163296 disk has a lower overall gas-phase methanol content with respect to formaldehyde than the TW Hya disk. In this section we discuss possible reasons for a lower methanol-to-formaldehyde ratio in HD 163296, as well as a brief assessment of the observing time needed to detect the low predicted abundances of gas-phase methanol in this disk.

### 4.1. CH$_3$OH/H$_2$CO in HD 163296 and TW Hya

It should be noted that there are uncertainties on the order of a factor of a few when deriving the methanol-to-formaldehyde ratio as described in this work. Namely, the column density calculation for the methanol detection in TW Hya is a result of three stacked line transitions rather than a single common transition as for H$_2$CO observed in both disks. The CH$_3$OH $3_{12}$–$3_{03}$ (A) line at 305.473 GHz is the strongest methanol line observed in TW Hya, but it is not the sole contributor to the detected line emission. However, even if all three lines are equally strong and the 305.473 GHz line contributes only 33% to the total stacked line intensity, then the inferred TW Hya value for CH$_3$OH/H$_2$CO of 0.42 is still higher than our upper limit for HD 163296 of <0.24. Matched filter analysis of the TW Hya CH$_3$OH detections (e.g., Fig. 7 in Loomis et al. 2018) shows that the CH$_3$OH $3_{12}$–$3_{03}$ (A) line is indeed stronger than the other two band seven lines used by Walsh et al. (2016) for line stacking, suggesting that a contribution of ∼50% to the stacked emission is a reasonable estimate.

Modeling by Willacy (2007) explores complex gas-grain chemical models of protoplanetary disks including H$_2$CO and CH$_3$OH with the following desorption processes: thermal desorption, desorption due to cosmic-ray heating of grains, and photodesorption. Their models, based on the UMIST Database for Astrochemistry network, show that outer disk abundances should give CH$_3$OH/H$_2$CO $\approx 0.04$, which is lower than both the ratio found for TW Hya and the upper limit on the ratio found for HD 163296. However, these models neglect radical–radical pathways to form larger complex organic molecules. Gas-grain chemical models by Semenov & Wiebe (2011) based

on the Ohio State University (OSU) network predict low column densities of methanol ice due to the high diffusion barrier used in the grain-surface chemistry, which highlights the importance of the assumed chemical parameters in these models. Their models and work by Furuya & Aikawa (2014) show that production of CH$_3$OH is sensitive to turbulent mixing and that the abundance of gas-phase CH$_3$OH, and thus the methanol-to-formaldehyde ratio, will increase when turbulent mixing is strong. The HD 163296 disk has a low degree of turbulence ≲0.05 $c_\mathrm{s}$ (Flaherty et al. 2015, 2017), while the TW Hya disk has similar low values of ≲0.05–0.10 $c_\mathrm{s}$ (Flaherty et al. 2018), suggesting vertical mixing is not strong in these disks.

Other recent work by Walsh et al. (2014) based on the OSU network investigates the production of complex molecules in disks, including H$_2$CO and CH$_3$OH, using an extensive full chemical network with chemical ingredients similar to the previously mentioned works. Their models include two-body, X-ray, and cosmic ray reactions and photoreactions in the gas phase and on grain surfaces as all as gas-grain reactions (e.g., freeze-out and photodesorption) around a T Tauri-like PMS star. The models in that work show that their outer disk ($R = 250$ AU) hosts a large methanol and formaldehyde ice reservoir with a sufficient number of these molecules released into the gas phase to give CH$_3$OH/H$_2$CO $\approx 0.33$. Subsequent work by Walsh et al. (2015) examines molecular complexity across different luminosities (M dwarf, T Tauri, Herbig Ae/Be) for the inner disk following a similar modeling approach. The authors find that molecular organics like H$_2$CO and CH$_3$OH contribute to the disk gas-phase carbon and oxygen reservoir for the cooler PMS stars, but not for the warmer Herbig Ae/Be PMS stars. These modeling results perhaps point to important differences in how these two molecules are formed in T Tauri disks versus Herbig Ae/Be disks.

The underlying physical structure in the TW Hya disk and the HD 163296 disk might explain the observed discrepancy between their methanol-to-formaldehyde ratios. Recent observations of submillimeter and scattered light in these disks highlight important differences in their dust structure. The micron-sized dust observed in scattered light is highly coupled to the gas and traces the surface layers of the disk, while millimeter-sized dust has mostly decoupled from the gas and settled toward the disk midplane (Dullemond & Dominik 2004; D'Alessio et al. 2006; Williams & Cieza 2011). The TW Hya disk was observed with ALMA in the band six continuum at 850 $\mu$m and with VLT/SPHERE in $H$-band at 1.62 $\mu$m (Andrews et al. 2016; van Boekel et al. 2017), showing several rings and gaps in both millimeter- and micron-sized dust. The micron-sized dust rings tracing the surface layers extend beyond the millimeter-sized dust in this disk. In contrast, recent scattered light observations by VLT/SPHERE in $H$-band, Keck/NIRC2 in $J$-band, and
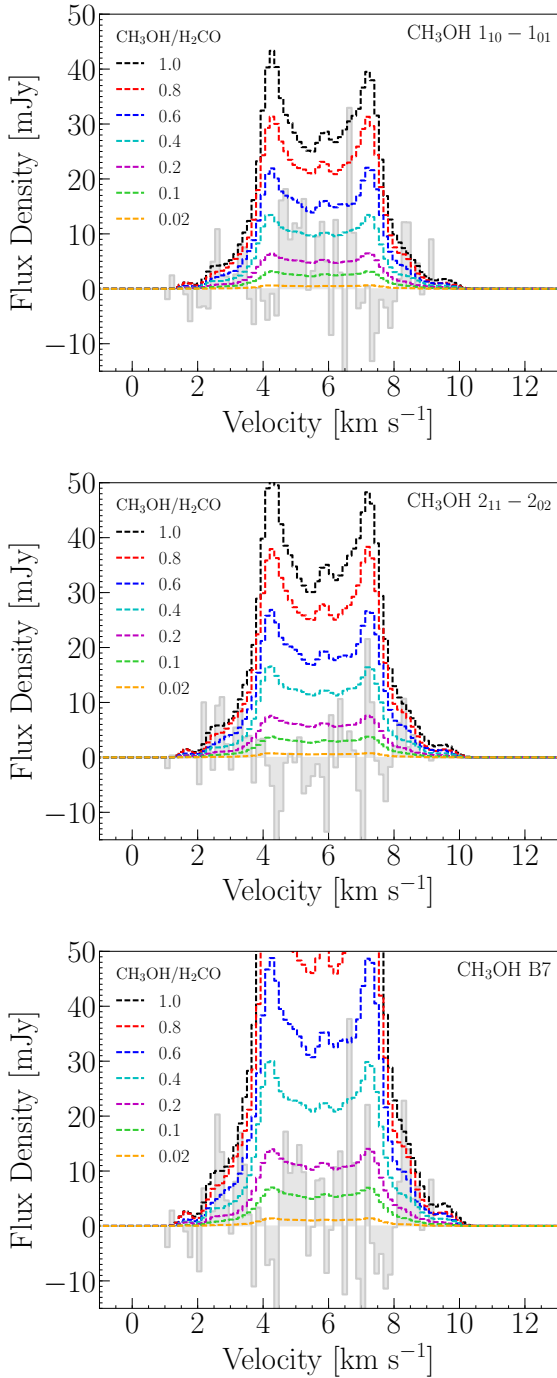
**Fig. 3.** Model $CH_3OH$ spectra at different methanol-to-formaldehyde abundance ratios (colored dashed lines) compared to the ALMA $CH_3OH$ non-detections after Keplerian masking (gray) in the HD 163296 disk. Given the sensitivity levels achieved, the ALMA observations should be sensitive to the presence of methanol in the disk for $CH_3OH/H_2CO \gtrsim 0.2$ based on the stacked band seven lines. *Top panel*: $CH_3OH$ $1_{10}-1_{01}$ (A) line. *Middle panel*: $CH_3OH$ $2_{11}-2_{02}$ (A) line. *Bottom panel*: stacked band seven $CH_3OH$ lines.

ALMA 1.3 mm observations of the HD 163296 disk show that no scattered light is observed beyond the innermost millimeter dust ring, suggesting that the surface layers of the outer disk are relatively flat and may be shadowed by the innermost dust ring (Muro-Arena et al. 2018; Guidi et al. 2018). Ultraviolet radiation from the central star can release molecular ices back into the gas phase via UV photodesorption (Öberg et al. 2009, 2015;

Huang et al. 2016), which may be suppressed if the HD 163296 outer disk is shadowed.

Alternatively, both disks may have a similar degree of UV irradiation, but as a Herbig Ae star HD 163296 will have a harder UV spectrum than TW Hya, which is dominated by Lyman-$\alpha$ emission (e.g., Fig. 1 in Walsh et al. 2015). The UV photodesorption rate of methanol ice is a strong function of photon energy and absorption cross section (Cruz-Diaz et al. 2016), and therefore will depend on the shape of the radiation field as well as the strength (Bertin et al. 2016). A harder, stronger Herbig Ae radiation field will lead to more $CH_3OH$ fragmentation upon photodesorption and thus methanol ice will be converted into other gas-phase species which could go on to seed $H_2CO$ formation in the gas phase.

Another possibility is that the HD 163296 disk formed from a protostar that did not inherit a large amount of methanol ice. Perhaps during formation, temperatures remained too warm for CO freeze-out needed to produce the high methanol-to-formaldehyde ice ratios seen in ISM ices. Chemical models with some methanol already formed at earlier stages (Walsh et al. 2014) host a more abundant methanol ice reservoir than models which start from atomic abundances, which have orders of magnitude lower methanol ice abundances (e.g., Molyarova et al. 2017).

While both formaldehyde and methanol are thought to be formed via hydrogenation of CO ices (Watanabe & Kouchi 2002), formaldehyde can also be formed in the gas phase. Recent chemical models by Agúndez et al. (2018) that do not include grain-surface chemistry are able to reproduce observed column densities of $H_2CO$, but not $CH_3OH$, in the outer regions of T Tauri and Herbig Ae/Be disks. Reactions between $CH_3$ and atomic oxygen can occur in the disk surface layers where oxygen-bearing species are photodissociated (Fockenberg & Preses 2002; Atkinson et al. 2006). This reaction, however, has not been shown to contribute significantly to the $H_2CO$ abundance in recent chemical models of disks around T Tauri stars (Walsh et al. 2014). The contribution may be larger in warmer, strongly irradiated disks around Herbig Ae/Be stars. Ion-molecule chemistry – which has a large influence on the gas-phase reservoir in the intermediate layers of protoplanetary disks – involving for example $HCO^+$, $H_3O^+$, and $H_3^+$ may also contribute to the overall gas-phase $H_2CO$ abundance (Vasyunin et al. 2008). It may be that the HD 163296 disk is particularly rich in $H_2CO$ formed in the gas phase, thus reducing its overall methanol-to-formaldehyde ratio. However, results from a recent analysis using the ortho-to-para ratio of $H_2CO$ as a tool to investigate its chemical origins are consistent with significant grain-surface formation and subsequent desorption (Guzmán et al. 2018). Detailed chemical models of the HD 163296 protoplanetary disk beyond the scope of this work are required to test and quantify the importance of the production and destruction routes for $H_2CO$ and $CH_3OH$ discussed here.

### 4.2. Detectability of methanol

We can estimate the required ALMA observing time for a $3\sigma$ detection of $CH_3OH$ in the HD 163296 disk given a range of $CH_3OH/H_2CO$ values consistent with our upper limit of <0.24. We considered methanol abundances relative to formaldehyde of 0.20, 0.10, 0.05, as these would be below our current $3\sigma$ upper limit of <0.24 listed in Table 3. To observe the $CH_3OH$ $2_{11}-2_{02}$ (A) line of methanol with similar spatial and spectral resolution at these assumed $CH_3OH/H_2CO$ values, we would need to increase our sensitivity by factors of about ~1.5, 2.5, and 5,

respectively. Because the telescope sensitivity is inversely proportional to the square root of the observing time, $\sigma_S \propto 1/\sqrt{t}$, the time required to realize these increases in sensitivity would multiply by factors of 2.25, 6.25, and 25, respectively. Based on the band seven observations presented here with 105 min of total on-source time, these factors translate to total on-source times of ~4, ~11, ~44 h for methanol at 20, 10, and 5% of the formaldehyde content in HD 163296, respectively. The detection of 10% methanol relative to formaldehyde is a clear practical limit for the HD 163296 disk based on these required integration times.

Disk size has a significant effect on methanol detectability. Using our HD 163296 model, we decreased the outer radius of the disk and scaled the disk physical structure (i.e., gas density and temperature) proportionally to test the effect of disk size on the band seven methanol line strengths for Herbig disks similar to HD 163296. The LIME models were rerun for an outer disk radius from $R_{out} = 100$–600 AU in steps of 50 AU for CH$_3$OH/H$_2$CO = 0.10. The disk-integrated line intensity for the band seven CH$_3$OH lines decreases by one order of magnitude for disks with $R_{out} = 250$ AU and by more than two orders of magnitude for disks with $R_{out} = 100$ AU. It is highly unlikely that methanol will be detected within an observing time of <20 h in most disks smaller than ~300 AU, considering the difficulty in detecting methanol relative to formaldehyde at the <25% level in the HD 163296 disk, which has a radius of ~550 AU and a proximity closer than most nearby star-forming regions. These results depend on the assumption that CH$_3$OH shares the same extended emitting area as H$_2$CO.

It may be that the methanol lines targeted in this work are not suitable candidates for disks around Herbig Ae/Be stars. The choice to target these four CH$_3$OH lines with ALMA in band six and band seven was motivated by the chemical modeling of a disk around a T Tauri star (Walsh et al. 2014) and by the methanol detection in the disk around TW Hya, also a T Tauri star (Walsh et al. 2016). Disks around Herbig Ae/Be stars are warmer, with a larger thermally desorbed inner reservoir due to the stronger stellar radiation. There is a potential reservoir of hot methanol in the inner disk atmosphere, similar to the hot water reservoir already observed in disks around less luminous T Tauri stars (Carr & Najita 2008; Salyk et al. 2008). Such emission could be compact yet still accessible in Herbig Ae/Be disks.

In summary, the CH$_3$OH lines in ALMA band seven presented here should be detectable in disks with CH$_3$OH/H$_2$CO as low as ~10% within realistic observing times, but only in disks with similar mass, size, distance, and H$_2$CO abundance as those found in the HD 163296 disk.

## 5. Conclusions

This paper presents ALMA observations targeting two CH$_3$OH lines in band six and two CH$_3$OH lines in band seven in the protoplanetary disk around HD 163296. We determine upper limits on the abundance of methanol likely to be present in the HD 163296 disk and compare to TW Hya, currently the only Class II disk with a positive detection of gas-phase methanol. The conclusions of this work are as follows:

- None of the four CH$_3$OH lines are detected in the disk around HD 163296 individually nor after line stacking. Upper limits on the integrated intensity at the $3\sigma$ level are <51 mJy km s$^{-1}$ for band six lines and <26 mJy km s$^{-1}$ for band seven lines. Neither aperture masking in the image plane, Keplerian masking in the image plane, nor matched filter analysis in the $uv$ plane recover any methanol emission,

indicating that our calculated $3\sigma$ upper limits are highly robust.
- The CH$_3$OH $2_{11}$–$2_{02}$ (A) line provides the strictest upper limit on the disk-averaged column density and abundance of methanol in the HD 163296 disk, with $N_{avg} < 5.0 \times 10^{11}$ cm$^{-2}$ and CH$_3$OH/H$_2 \lesssim 1.6 \times 10^{-12}$ at the $3\sigma$ level.
- The upper limit on the methanol-to-formaldehyde ratio in the HD 163296 disk is CH$_3$OH/H$_2$CO < 0.24 at the $3\sigma$ level. This ratio is lower than that of the TW Hya disk at CH$_3$OH/H$_2$CO = 1.27 ± 0.13, indicating that the HD 163296 disk has a low amount methanol with respect to formaldehyde relative to the TW Hya disk.
- Possible explanations for the lower methanol-to-formaldehyde ratio in HD 163296 include: a low amount of gas-phase methanol is desorbed from icy grains at the disk midplane due to the flatter, shadowed disk geometry as seen in recent images taken by VLT/SPHERE; differences in the desorption processes in the HD 163296 disk compared to the TW Hya disk; and a higher-than-expected gas-phase formaldehyde abundance, as H$_2$CO may also be formed in the gas phase in the disk upper layers.
- To detect methanol at the $3\sigma$ level in the HD 163296 disk, we estimate that it is necessary to increase the total on-source observing time with the full ALMA 12-meter array up to 4 h to be sensitive to CH$_3$OH/H$_2$CO ≈ 20% and up to 11 h to be sensitive to CH$_3$OH/H$_2$CO ≈ 10%. These estimates apply to other Herbig Ae/Be disks with masses, sizes, and distances similar to that found for the HD 163296 disk.

## References

Agúndez, M., Roueff, E., Le Petit, F., & Le Bourlot, J. 2018, A&A, 616, A19
Aikawa, Y., Momose, M., Thi, W.-F., et al. 2003, PASJ, 55, 11
Alecian, E., Wade, G. A., Catala, C., et al. 2013, MNRAS, 429, 1001
Andrews, S. M., Wilner, D. J., Zhu, Z., et al. 2016, ApJ, 820, L40
Atkinson, R., Baulch, D. L., Cox, R. A., et al. 2006, Atm. Chem. Phys., 6, 3625
Bergin, E. A., Cleeves, L. I., Gorti, U., et al. 2013, Nature, 493, 644
Bertin, M., Romanzin, C., Doronin, M., et al. 2016, ApJ, 817, L12
Boogert, A. C. A., Gerakines, P. A., & Whittet, D. C. B. 2015, ARA&A, 53, 541
Bottinelli, S., Boogert, A. C. A., Bouwman, J., et al. 2010, ApJ, 718, 1100
Brinch, C., & Hogerheijde, M. R. 2010, A&A, 523, A25
Carney, M. T., Hogerheijde, M. R., Loomis, R. A., et al. 2017, A&A, 605, A21
Carr, J. S., & Najita, J. R. 2008, Science, 319, 1504
Collings, M. P., Anderson, M. A., Chen, R., et al. 2004, MNRAS, 354, 1133
Cruz-Diaz, G. A., Martín-Doménech, R., Muñoz Caro, G. M., & Chen, Y.-J. 2016, A&A, 592, A68
Cuppen, H. M., van Dishoeck, E. F., Herbst, E., & Tielens, A. G. G. M. 2009, A&A, 508, 275
D'Alessio, P., Calvet, N., Hartmann, L., Franco-Hernández, R., & Servín, H. 2006, ApJ, 638, 314
Dartois, E., Schutte, W., Geballe, T. R., et al. 1999, A&A, 342, L32
de Gregorio-Monsalvo, I., Ménard, F., Dent, W., et al. 2013, A&A, 557, A133

Drozdovskaya, M. N., Walsh, C., Visser, R., Harsono, D., & van Dishoeck E. F. 2014, MNRAS, 445, 913

Dullemond, C. P., & Dominik, C. 2004, A&A, 421, 1075

Flaherty, K. M., Hughes, A. M., Rosenfeld, K. A., et al. 2015, ApJ, 813, 99

Flaherty, K. M., Hughes, A. M., Rose, S. C., et al. 2017, ApJ, 843, 150

Flaherty, K. M., Hughes, A. M., Teague, R., et al. 2018, ApJ, 856, 117

Fockenberg, C., & Preses, J. M. 2002, J. Phys. Chem. A, 106, 2924

Friberg, P., Madden, S. C., Hjalmarson, A., & Irvine, W. M. 1988, A&A, 195, 281

Furuya, K., & Aikawa, Y. 2014, ApJ, 790, 97

Gaia Collaboration (Brown, A. G. A., et al.) 2018, A&A, 616, A1

Garrod, R. T., & Herbst, E. 2006, A&A, 457, 927

Graninger, D. M., Wilkins, O. H., & Öberg, K. I. 2016, ApJ, 819, 140

Grim, R. J. A., Baas, F., Geballe, T. R., Greenberg, J. M., & Schutte, W. A. 1991, A&A, 243, 473

Guidi, G., Ruane, G., Williams, J. P., et al. 2018, MNRAS, 479, 1505

Guzmán, V. V., Öberg, K. I., Carpenter, J., et al. 2018, ApJ, 864, 170

Herbst, E., & van Dishoeck, E. F. 2009, ARA&A, 47, 427

Huang, J., Öberg, K. I., & Andrews, S. M. 2016, ApJ, 823, L18

Isella, A., Guidi, G., Testi, L., et al. 2016, Phys. Rev. Lett., 117, 251101

Kristensen, L. E., van Dishoeck, E. F., van Kempen, T. A., et al. 2010, A&A, 516, A57

Lee, C.-F., Li, Z.-Y., Ho, P. T. P., et al. 2017, ApJ, 843, 27

Loomis, R. A., Cleeves, L. I., Öberg, K. I., Guzman, V. V., & Andrews, S. M. 2015, ApJ, 809, L25

Loomis, R. A., Öberg, K. I., Andrews, S. M., et al. 2018, AJ, 155, 182

Mathews, G. S., Klaassen, P. D., Juhász, A., et al. 2013, A&A, 557, A132

McMullin, J. P., Waters, B., Schiebel, D., Young, W., & Golap, K. 2007, in Astronomical Data Analysis Software and Systems XVI, eds. R. A. Shaw, F. Hill, & D. J. Bell, ASP Conf. Ser., 376, 127

Miao, Y., Mehringer, D. M., Kuan, Y.-J., & Snyder, L. E. 1995, ApJ, 445, L59

Molyarova, T., Akimkin, V., Semenov, D., et al. 2017, ApJ, 849, 130

Müller, H. S. P., Schlöder, F., Stutzki, J., & Winnewisser, G. 2005, J. Mol. Struct., 742, 215

Muro-Arena, G. A., Dominik, C., Waters, L. B. F. M., et al. 2018, A&A, 614, A24

Öberg, K. I., Garrod, R. T., van Dishoeck, E. F., & Linnartz, H. 2009, A&A, 504, 891

Öberg, K. I., Qi, C., Fogel, J. K. J., et al. 2010, ApJ, 720, 480

Öberg, K. I., Furuya, K., Loomis, R., et al. 2015, ApJ, 810, 112

Öberg, K. I., Guzmán, V. V., Merchantz, C. J., et al. 2017, ApJ, 839, 43

Pinte, C., Price, D. J., Ménard, F., et al. 2018, ApJ, 860, L13

Pontoppidan, K. M., van Dishoeck, E. F., & Dartois, E. 2004, A&A, 426, 925

Qi, C., D'Alessio, P., Öberg, K. I., et al. 2011, ApJ, 740, 84

Qi, C., Öberg, K. I., & Wilner, D. J. 2013, ApJ, 765, 34

Qi, C., Öberg, K. I., Andrews, S. M., et al. 2015, ApJ, 813, 128

Rabli, D., & Flower, D. R. 2010, MNRAS, 406, 95

Remijan, A., Snyder, L. E., Friedel, D. N., Liu, S.-Y., & Shah, R. Y. 2003, ApJ, 590, 314

Rosenfeld, K. A., Andrews, S. M., Hughes, A. M., Wilner, D. J., & Qi, C. 2013, ApJ, 774, 16

Salinas, V. N., Hogerheijde, M. R., Mathews, G. S., et al. 2017, A&A, 606, A125

Salyk, C., Pontoppidan, K. M., Blake, G. A., et al. 2008, ApJ, 676, L49

Semenov, D., & Wiebe, D. 2011, ApJS, 196, 25

Shimonishi, T., Onaka, T., Kato, D., et al. 2010, A&A, 514, A12

Skinner, C. J., Tielens, A. G. G. M., Barlow, M. J., & Justtanont, K. 1992, ApJ, 399, L79

Teague, R., Bae, J., Bergin, E. A., Birnstiel, T., & Foreman-Mackey, D. 2018, ApJ, 860, L12

van Boekel, R., Henning, T., Menu, J., et al. 2017, ApJ, 837, 132

van den Ancker, M. E., de Winter, D., & Tjin A Djie, H. R. E. 1998, A&A, 330, 145

van der Marel, N., van Dishoeck, E. F., Bruderer, S., & van Kempen, T. A. 2014, A&A, 563, A113

van Dishoeck, E. F., Blake, G. A., Jansen, D. J., & Groesbeck, T. D. 1995, ApJ, 447, 760

van 't Hoff, M. L. R., Tobin, J. J., Trapman, L., et al. 2018, ApJ, 864, L23

Vasyunin, A. I., Semenov, D., Henning, T., et al. 2008, ApJ, 672, 629

Walsh, C., Millar, T. J., Nomura, H., et al. 2014, A&A, 563, A33

Walsh, C., Nomura, H., & van Dishoeck E. 2015, A&A, 582, A88

Walsh, C., Loomis, R. A., Öberg, K. I., et al. 2016, ApJ, 823, L10

Watanabe, N., & Kouchi, A. 2002, ApJ, 571, L173

Watanabe, N., Shiraki, T., & Kouchi, A. 2003, ApJ, 588, L121

Wiesenfeld, L., & Faure, A. 2013, MNRAS, 432, 2573

Willacy, K. 2007, ApJ, 660, 441

Williams, J. P., & Cieza, L. A. 2011, ARA&A, 49, 67

## Appendix A: Molecular abundances for different $T_{ex}$

Here the disk-averaged column densities and abundances are shown for CH$_3$OH and H$_2$CO in the disk around HD 163296 and the disk around TW Hya for different excitation temperatures $T_{ex}$. The method used is described in Sect. 3.2.

Equation (1) assumes optically thin emission and LTE excitation conditions. The excitation temperature $T_{ex}$ was set to 25, 50 and 75 K, indicating different regions of the disk from which the emission lines may originate. At most, differences of factors 2–3 are seen in the disk-averaged column density and abundance for the values of $T_{ex}$ explored here.

**Table A.1.** Disk-averaged column density and abundance of CH$_3$OH and H$_2$CO in HD 163296 and TW Hya for varying $T_{ex}$.

| Object | Line | $\int I_\nu d\nu^a$ (mJy km s$^{-1}$) | $E_u$ (K) | log($A_{ul}$) (s$^{-1}$) | $T_{ex}$ (K) | $n_{crit}$ (cm$^{-3}$) | $N_{avg}$ (cm$^{-2}$) | CH$_3$OH/H$_2$ | CH$_3$OH/H$_2$CO$^b$ |
|---|---|---|---|---|---|---|---|---|---|
| | | | | CH$_3$OH | | | | | |
| HD 163296 | CH$_3$OH $5_{05}$–$4_{04}$ (E) | <51 | 47.9 | −4.22 | 25 | 1.6(06) | <6.9(12) | <2.1(−11) | |
| | | | | | 50 | 1.9(06) | <8.6(12) | <2.6(−11) | |
| | | | | | 75 | 2.1(06) | <1.1(13) | <3.5(−11) | |
| | CH$_3$OH $5_{05}$–$4_{04}$ (A) | <51 | 34.8 | −4.22 | 25 | 4.3(05) | <4.1(12) | <1.3(−11) | |
| | | | | | 50 | 5.0(05) | <6.6(12) | <2.0(−11) | |
| | | | | | 75 | 5.0(05) | <9.6(13) | <3.0(−11) | |
| | CH$_3$OH $1_{10}$–$1_{01}$ (A) | <26 | 16.9 | −3.49 | 25 | 4.3(07) | <7.0(11) | <2.2(−12) | |
| | | | | | 50 | 5.6(07) | <1.6(12) | <5.0(−12) | |
| | | | | | 75 | 6.4(07) | <2.7(12) | <8.2(−12) | |
| | CH$_3$OH $2_{11}$–$2_{02}$ (A) | <26 | 21.6 | −3.49 | 25 | 5.0(06) | <5.0(11) | <1.6(−12) | |
| | | | | | 50 | 5.4(06) | <1.1(12) | <3.3(−12) | |
| | | | | | 75 | 5.5(06) | <1.7(12) | <5.2(−12) | |
| TW Hya | CH$_3$OH stacked$^c$ | 26.5 ± 2.7 | 28.6 | −3.49 | 25 | 3.0(06) | 4.7(12) | 1.1(−12) | |
| | | | | | 50 | 3.0(06) | 8.6(12) | 2.1(−12) | |
| | | | | | 75 | 3.1(06) | 1.3(13) | 3.2(−12) | |
| | | | | H$_2$CO | | | | | |
| HD 163296 | H$_2$CO $3_{12}$–$2_{11}$ | 890 ± 89 | 33.4 | −3.55 | 25 | 5.7(06) | 2.1(12) | 6.3(−12) | <0.24 |
| | | | | | 50 | 6.2(06) | 3.0(12) | 9.2(−12) | <0.43 |
| | | | | | 75 | 6.4(06) | 4.2(12) | 1.3(−11) | <0.50 |
| TW Hya | H$_2$CO $3_{12}$–$2_{11}$ | 291 ± 29 | 33.4 | −3.55 | 25 | 5.7(06) | 3.7(12) | 8.9(−13) | 1.27 ± 0.13 |
| | | | | | 50 | 6.2(06) | 5.3(12) | 1.6(−12) | 1.62 ± 0.16 |
| | | | | | 75 | 6.4(06) | 7.5(12) | 1.8(−12) | 1.73 ± 0.17 |

**Notes.** The format $a(b)$ translates to $a \times 10^b$. Flux errors are dominated by systematic uncertainties, taken to be 10%. [a] Upper limits are derived at the 3$\sigma$ level using the HD 163296 Keplerian mask (Sect. 3). [b] Ratios are determined using the CH$_3$OH disk-integrated column density from Table 2. HD 163296: based on the strictest upper limit from the CH$_3$OH $2_{11}$–$2_{02}$ (A) line. TW Hya: based on the stacked CH$_3$OH detection. [c] The stacked detection consists of three CH$_3$OH transitions: CH$_3$OH $2_{11}$–$2_{02}$ (A) at 304.208 GHz, CH$_3$OH $3_{12}$–$3_{03}$ (A) at 305.472 GHz, and CH$_3$OH $4_{13}$–$4_{04}$ at 307.166 GHz. Excitation parameters for the CH$_3$OH $3_{12}$–$3_{03}$ (A) line are used to calculate column density.
**References.** Rabli & Flower (2010); Wiesenfeld & Faure (2013); Walsh et al. (2016); Qi et al. (2013); Öberg et al. (2017).